

Layered rare-earth hydroxide and oxide nanoplates of the Y/Tb/Eu system: phase-controlled processing, structure characterization and color-tunable photoluminescence via selective excitation and efficient energy transfer

Xiaoli Wu^{1,2}, Ji-Guang Li^{1,2}, Jinkai Li¹, Qi Zhu¹, Xiaodong Li¹, Xudong Sun¹ and Yoshio Sakka²

¹ Key Laboratory for Anisotropy and Texture of Materials (Ministry of Education), School of Materials and Metallurgy, Northeastern University, Shenyang, Liaoning 110004, China

² Advanced Materials Processing Unit, National Institute for Materials Science, Sengen 1-2-1, Tsukuba, Ibaraki 305-0047, Japan

E-mail: LI.Jiguang@nims.go.jp

Received 11 September 2012

Accepted for publication 22 January 2013


Published 21 February 2013

Online at stacks.iop.org/STAM/14/015006

Abstract

Well-crystallized $(Y_{0.97-x}Tb_{0.03}Eu_x)_2(OH)_5NO_3 \cdot nH_2O$ ($x = 0-0.03$) layered rare-earth hydroxide (LRH) nanoflakes of a pure high-hydration phase have been produced by autoclaving from the nitrate/ NH_4OH reaction system under the optimized conditions of $100^\circ C$ and $pH \sim 7.0$. The flakes were then converted into $(Y_{0.97-x}Tb_{0.03}Eu_x)_2O_3$ phosphor nanoplates with color-tunable photoluminescence. Detailed structural characterizations confirmed that LRH solid solutions contained NO_3^- anions intercalated between the layers. Characteristic Tb^{3+} and Eu^{3+} emissions were detected in the ternary LRHs by selectively exciting the two types of activators, and the energy transfer from Tb^{3+} to Eu^{3+} was observed. Annealing the LRHs at $1100^\circ C$ produced cubic-lattice $(Y_{0.97-x}Tb_{0.03}Eu_x)_2O_3$ solid-solution nanoplates with exposed 222 facets. Multicolor, intensity-adjustable luminescence was attained by varying the excitation wavelength from ~ 249 nm (the charge transfer excitation band of Eu^{3+}) to 278 nm (the $4f^8-4f^75d^1$ transition of Tb^{3+}). Utilizing the efficient Tb^{3+} to Eu^{3+} energy transfer, the emission color of $(Y_{0.97-x}Tb_{0.03}Eu_x)_2O_3$ was tuned from approximately green to yellowish-orange by varying the Eu^{3+}/Tb^{3+} ratio. At the optimal Eu^{3+} content of $x = 0.01$, the efficiency of energy transfer was $\sim 91\%$ and the transfer mechanism was suggested to be electric multipole interactions. The phosphor nanoplates developed in this work may be incorporated in luminescent films and find various lighting and display applications.

Keywords: layered rare-earth hydroxide, solid solution, color-tunable luminescence, energy transfer

 Online supplementary data available from stacks.iop.org/STAM/14/015006/mmedia



Content from this work may be used under the terms of the [Creative Commons Attribution-NonCommercial-ShareAlike 3.0 licence](http://creativecommons.org/licenses/by-nc-sa/3.0/). Any further distribution of this work must maintain attribution to the author(s) and the title of the work, journal citation and DOI.

1. Introduction

Rare-earth elements are used in phosphors for fluorescent lamps, white-light-emitting diodes, plasma display panels, flat-panel displays, field emission displays, and cathode-ray tubes. Current advances in high-definition display technologies require fine phosphor particles of well-defined morphology to improve the resolution by reducing pixel size, improve the overall luminescent performance and reduce the size of optoelectronic devices. As the traditional solid-state reaction route generally yields micron-sized phosphor particles with a wide size distribution and considerable aggregation [1], the past decade witnessed a boom in solution-based processing of phosphor particles with better-defined characteristics [2–7]. Y_2O_3 doped with Eu^{3+} and Tb^{3+} ions are among the best-known red-emitting and green-emitting phosphors, respectively, owing to their simple chemical composition, excellent luminescence efficiency, high color purity and long-term stability [8–10]. Tb^{3+} has also been used as a sensitizer to enhance Eu^{3+} emission in some phosphor systems such as $\text{Y}_2\text{O}_2\text{S}:\text{Eu}^{3+}$ [11]. Among the low-dimensional $\text{Y}_2\text{O}_3:\text{RE}$ phosphors (RE = rare-earth element), zero-dimensional (0D) nanoparticles [12–14] and 1D nanowires/nanotubes [15–19] have been extensively studied for their controlled synthesis, surface modification, size and shape dependent optical properties, and new applications in areas such as bio-analysis [20]. However, reports on 2D nanosheets were rare. In the solution-based processing methodology, oxide phosphors are mostly produced via controlled precursor synthesis followed by proper annealing. The lack of studies on 2D nanophosphors originated from the scarcity of precursor nanosheets or precursor compounds that could be delaminated into nanosheets. A breakthrough came in 2006 [21] when Gandara *et al* synthesized interlayer-anion exchangeable layered rare-earth hydroxides (LRHs) of the typical composition $\text{Ln}_2(\text{OH})_5\text{A} \cdot n\text{H}_2\text{O}$, where A is interlayer anion such as NO_3^- , Cl^- or Br^- ; Ln is lanthanide (but may also be Y); and $n = 1.5\text{--}1.8$. Since then, considerable attention has been paid to LRHs owing to the interesting magnetic, catalytic and optical properties of the Ln elements. It was found that the LRH compounds tend to crystallize under roughly neutral pH, either through hydrothermal or refluxing synthesis, and the presence of mineralizers containing anion A helps stabilize the corresponding LRH phase [22–28]. Detailed crystal structure analysis by Sasaki *et al* [26] revealed two types of coordination environments for Ln^{3+} , that is, eight-fold coordinated $[\text{Ln}(\text{OH})_7(\text{H}_2\text{O})]$ (C_1 symmetry) and nine-fold coordinated $[\text{Ln}(\text{OH})_8(\text{H}_2\text{O})]$ (C_{4v} symmetry) polyhedrons. In the LRH structure, each LnO_8 unit is linked to two other LnO_8 and four LnO_9 groups via edge sharing. The linked polyhedron units form a two-dimensional host layer parallel to the *ab* plane, with the free anions A located in the interlayer to support the layers and for charge balance. Photoluminescence studies on the Y/Eu binary [29] and Y/Gd/Eu ternary [30] LRH systems showed that the optical properties crucially depend on the local symmetry around Eu^{3+} ions. Luminescence systematically changes with the

dehydration of LRH (decreasing n value), since the loss of crystal water shifts the Eu^{3+} symmetry from C_{4v} to C_1 [29]. It was also found that in the Y/Gd/Eu ternary system Gd^{3+} preferentially sensitizes the emission of Eu^{3+} ions possessing C_1 local symmetry [30].

Since the host layer of LRH is a close-packed (low energy) crystal plane, the LRH compounds tend to crystallize as nanoplates. The 2D morphologies of the pristine and the exfoliated LRHs are thus well suited for the construction of highly [001] oriented films with improved luminescence, since the [001] orientation maximizes the exposure of Ln activators to the excitation light [31–34]. Meanwhile, the [001] oriented LRH film would transform into a [111] oriented oxide film via quasitopotactic atomic arrangements under proper annealing [31–33], which should result in an enhanced exposure of the close-packed 222 facets of the oxide crystals and thus stronger luminescence [32–34]. Improved catalytic performance may similarly be expected from the maximized Ln exposure.

In view of the importance and wide application of $\text{Y}_2\text{O}_3:\text{Eu}^{3+}$ red and $\text{Y}_2\text{O}_3:\text{Tb}^{3+}$ green phosphors, Y/Tb binary and Y/Tb/Eu ternary LRHs were synthesized in this work for optical studies of the LRHs and their annealing-derived oxide nanoplates. With Eu^{3+} incorporation, color-tunable photoluminescence was achieved either by varying the excitation wavelength or through an efficient energy transfer from Tb^{3+} to Eu^{3+} ions. In the following sections, we report the phase purity controlled synthesis, detailed structure characterization and optical properties of the LRH compounds and their calcination-derived oxides.

2. Experimental procedures

2.1. Hydrothermal synthesis of LRH solid solutions

The starting rare-earth sources were Ln_2O_3 (Ln = Y, Tb and Eu; 99.99% purity; Conghua Jianfeng Rare Earth Co. Ltd, Conghua, China). Nitrate solutions of Ln^{3+} ions were prepared by dissolving the corresponding oxides with a proper amount of hot nitric acid. For each synthesis run, the total Ln^{3+} concentration was kept at 0.08 mol l^{-1} . Optimal Tb concentration in the $\text{Y}_2\text{O}_3:\text{Tb}^{3+}$ green phosphor was previously established at 5 at.% [35, 36], and in this work the Tb/(Y + Tb + Eu) atomic ratio was fixed at 3 at.%. The Eu content in the $(\text{Y}_{0.97-x}\text{Tb}_{0.03}\text{Eu}_x)$ combination was varied in the range of $x = 0\text{--}0.03$ to reveal its effects on the optical properties. In a typical synthesis, a proper amount of ammonium hydroxide solution (25 wt%) was added to the mixed nitrate solution until $\text{pH} \sim 7$, and the resultant suspension was then transferred into a Teflon-lined stainless steel autoclave after room-temperature homogenization for 30 min under magnetic stirring. The tightly sealed autoclave was placed in an electric oven preheated to a certain temperature in the range of $100\text{--}220^\circ\text{C}$ for a reaction period of 24 h. After natural cooling, the hydrothermal product was collected via centrifugation, washed with distilled water and ethanol, and finally dried in the air at 70°C for 24 h to yield a white powder for characterization and further processing.

2.2. Characterization techniques

Crystalline phases were identified with an x-ray diffractometer (XRD, Model RINT 2200 V/PC, Rigaku, Tokyo, Japan) operated at 40 kV per 40 mA, using nickel-filtered Cu-K α radiation and a scanning speed of 1°2 θ per minute. Fourier transform infrared spectroscopy (FTIR, Model 4200, JASCO, Tokyo) measurements were performed using KBr pellets. Morphology and microstructure were analyzed by transmission electron microscopy (TEM, 200 kV, Model JEM-2000FX, JEOL, Tokyo) and field emission scanning electron microscopy (FE-SEM, 10 kV, Model S-5000, Hitachi, Tokyo). Differential thermal analysis/thermogravimetry (DTA/TG, Model Thermo Plus TG8120, Rigaku, Tokyo) of the LRHs was carried out in stagnant air with a heating rate of 10 °C min⁻¹. Photoluminescence (PL), photoluminescence excitation (PLE) and fluorescence decay were analyzed at room temperature using an FP-6500 spectrofluorometer (JASCO, Tokyo) equipped with a 60 mm-diameter integrating sphere (Model ISF-513, JASCO) and a 150 W Xe lamp as the excitation source. Excitation and emission beams were monochromatized with a Rowland concave grating (1800 grooves mm⁻¹). Optical measurements were conducted at a scanning speed of 100 nm min⁻¹, wavelength accuracy of ± 0.3 nm and slit widths of 5 nm both in excitation and emission. Spectral response of the system was corrected in the range of 220–850 nm with a Rhodamine-B solution (5.5 g l⁻¹ in ethylene glycol) and a standard light source unit (ECS-333, JASCO) as references.

3. Results and discussion

3.1. Phase-controlled processing, structure characterization and optical properties of the Y/Tb/Eu LRHs

The LRH phase was widely observed to crystallize under approximately neutral pH [22–30]. When keeping solution pH at ~ 7.0 , we found that processing temperature significantly affects the phase composition of the hydrothermal product, as shown in figure 1 for the example of Y_{0.965}Tb_{0.03}Eu_{0.005} system. The sample synthesized at 100 °C exhibits a series of strong 00*l* and sharp 220 diffractions, suggesting that a Ln₂(OH)₅NO₃·*n*H₂O LRH compound with highly ordered host layers has been formed [21–34, 37–40]. The samples processed at higher temperatures up to 200 °C similarly show the 220 diffraction of LRH, but splitting of the 002 and 004 diffractions was clearly observed. Lattice spacing calculations (table S1; see the supplementary material available from stacks.iop.org/STAM/14/015006/mmedia) confirmed that the two additional peaks belong to oscillation diffractions in each case. The above results thus imply that these higher-temperature samples contain two phases with different interlayer distances. Dehydration was believed to be responsible for the appearance of the LRH phase with a shorter interlayer distance. Sasaki and co-workers [26–28] revealed that, in the LRH structure, water molecules are directly coordinated to the Ln atoms to form coordination polyhedrons, instead of being intercalated between the layers,

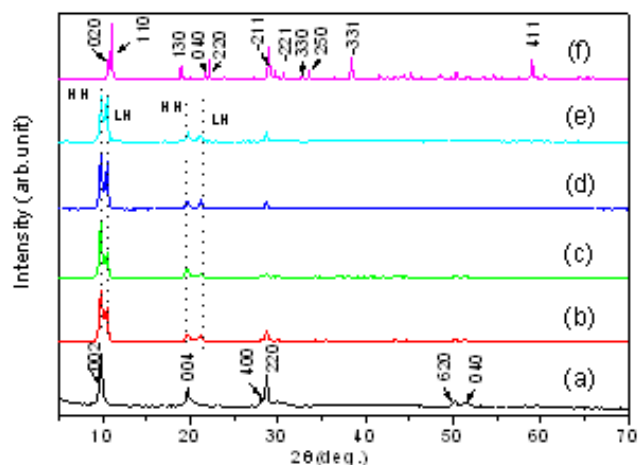


Figure 1. Powder XRD patterns of the hydrothermal products fabricated at (a) 100, (b) 130, (c) 150, (d) 180, (e) 200 and (f) 220 °C. All samples have the same cation combination of Y_{0.965}Tb_{0.03}Eu_{0.005}; HH and LH represent high-hydration and low-hydration phases, respectively.

and the loss of hydration water shortens the interlayer distance. This explanation was confirmed by water content analysis of the samples (figure S1). The LRH phase dehydrates up to ~ 260 °C [29, 30], and the average water contents derived from the TG curves at 260 °C indeed tend to decrease toward a higher synthesis temperature (table S1). The two phases are thereafter referred to high hydration (HH, larger interlayer spacing) and low hydration (LH) phases. The LH content can be evaluated from the intensities of the 002 diffractions of the HH (I_{HH002}) and LH (I_{LH002}) phases using the ratio $I_{LH002}/(I_{HH002} + I_{LH002})$. Results show that the samples synthesized at 130, 150, 180 and 200 °C have ~ 40.2 , 31.2, 45.8 and 49.2 wt% of the LH phase, respectively. Though the LH fraction tends to increase for a higher processing temperature, attempts to obtain a pure LH phase failed, as already at 220 °C the product changed into an anhydrous Ln₄O(OH)₉NO₃ compound (JCPDS file no. 79-1352, figure 1(f)).

FTIR spectra (figure S2) of the 100 °C sample show a single and sharp absorption band centered at ~ 1387 cm⁻¹, characteristic of free nitrate ions (the ν_3 vibration mode) in the interlayer of LRHs [21–28, 37, 41, 42]. The additional absorption at ~ 3600 cm⁻¹ is indicative of the hydroxide anion (OH⁻) [38, 39], while the 3380 and 1640 cm⁻¹ peaks can be assigned to the O–H stretching vibrations (ν_1 and ν_3) and the H–O–H bending mode (ν_2) of the water molecules, respectively [38, 39]. This analysis reveals that an LRH compound has been crystallized with free NO₃⁻ anions intercalated between the layers, in agreement with the XRD results. Although a shortened interlayer spacing might lead to the coordination of NO₃⁻ anions to Ln in the LH phase, FTIR spectra of the samples processed up to 200 °C exhibit the single absorption of free NO₃⁻ anion at ~ 1387 cm⁻¹, and are clearly different from the spectrum of the Ln₄O(OH)₉NO₃ compound obtained at 220 °C (spectrum d in figure S2). Since the nitrate anions are indirectly linked to Ln via the hydrogen bonding between OH⁻ and NO₃⁻

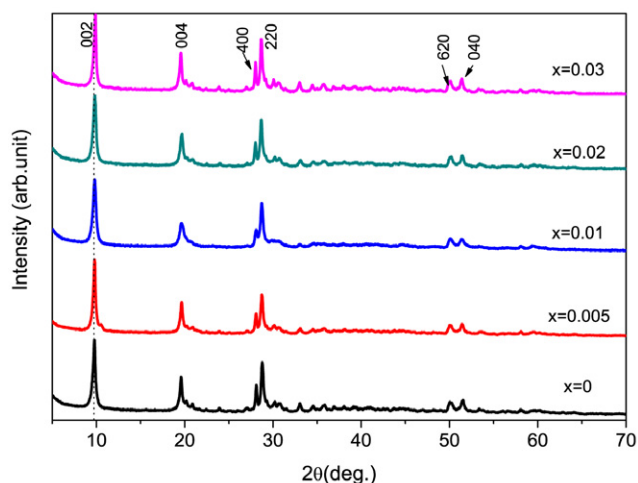


Figure 2. Powder XRD patterns of the $Y_{0.97-x}Tb_{0.03}Eu_x$ LRH samples synthesized at 100 °C.

anions in $Ln_4O(OH)_9NO_3$ [37], two peaks appear at ~ 1370 and 1410 cm^{-1} , corresponding to the ν_3 vibration of NO_3^- anion and the ν_4 asymmetric stretching of the O- NO_2 group, respectively [37, 41, 42].

FE-SEM observation indicated that the product obtained at 100 °C crystallizes as hexagonal nanoflakes with lateral sizes of up to ~ 500 nm and thicknesses of up to 80 nm (figure S3). Raising the hydrothermal temperature yields larger crystallites, and at 150 °C some crystallites of up to $\sim 2\ \mu\text{m}$ in lateral size and over 150 nm in thickness were produced. For the sake of phase purity, however, 100 °C was chosen as the hydrothermal temperature for the further synthesis.

Figure 2 shows XRD patterns of the powders synthesized at 100 °C, with varying x in the $Y_{0.97-x}Tb_{0.03}Eu_x$ combination. The strong $00l$ and 220 diffractions imply that well-crystallized LRHs have been produced. Splitting of the $00l$ diffractions was no longer observed in any sample. Closer observations revealed that the $00l$ diffractions slightly shift to the high-angle side and the 220 diffraction to the low-angle side with increasing Eu^{3+} concentration. As the $00l$ diffractions reflect the stacking of host layers along the c -axis of the crystal structure while the 220 diffraction originates within the host layers, the above results thus suggest that the interlayer distance shrinks while the ab plane expands at a higher Eu^{3+} content. The 002 basal spacing and 220 lattice spacing calculated from the XRD patterns are shown in table S2 (see the supplementary material available from stacks.iop.org/STAM/14/015006/mmedia). The shrinking interlayer distance is again caused by lowered hydration, as seen from the n value (table S2) derived via TG analysis (figure S4). Sasaki and co-workers [26–28] reported that, for the nitrate family of LRH, the hydration number n in $Ln_2(OH)_5NO_3 \cdot nH_2O$ decreases for a bigger Ln^{3+} ion, and this accounts for the successively lower hydration with increasing Eu^{3+} incorporation. We have reported similar phenomena in the Y/Eu binary [29] and Y/Gd/Eu ternary [30] nitrate-LRH systems. The expansion of the ab plane (host layer) results from

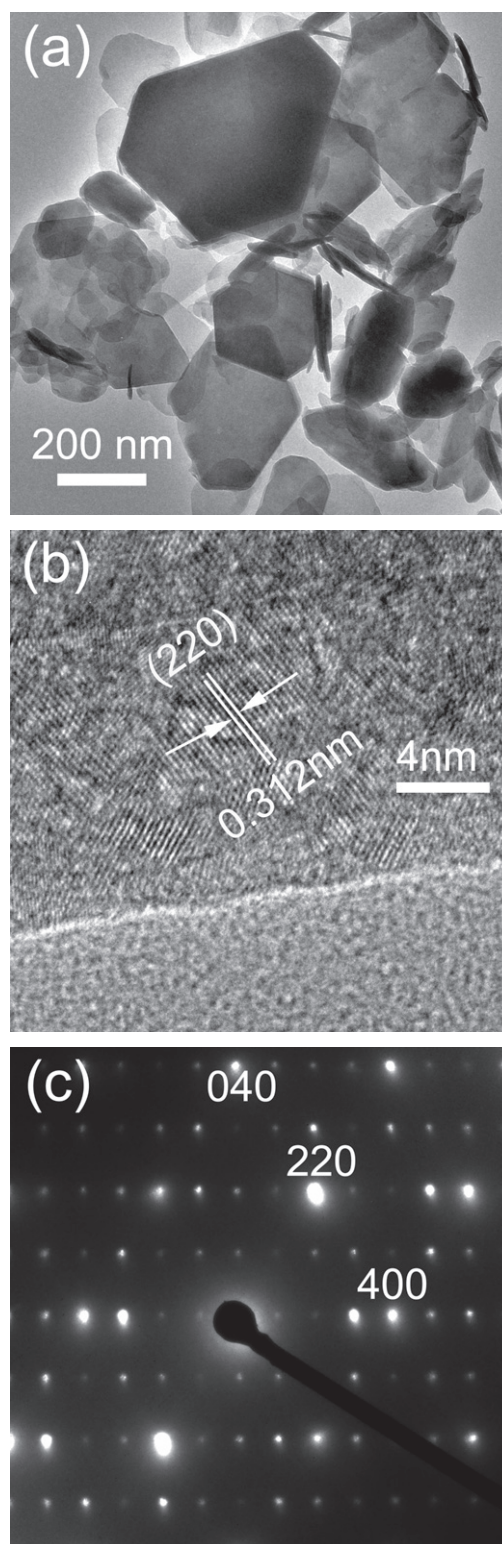


Figure 3. Low-magnification TEM (a) and HR-TEM (b) images and SAED pattern (c) of the $Y_{0.965}Tb_{0.03}Eu_{0.005}$ LRH.

the incorporation of relatively large Eu^{3+} ions (for eight-fold coordination, $r_{Y^{3+}} = 0.1019$, $r_{Tb^{3+}} = 0.1040$ and $r_{Eu^{3+}} = 0.1066$ nm; for nine-fold coordination, $r_{Y^{3+}} = 0.1075$, $r_{Tb^{3+}} = 0.1095$ and $r_{Eu^{3+}} = 0.1120$ nm) [43]. These results demonstrate that well-crystallized Y/Tb/Eu LRHs have been produced in the solid solution form.

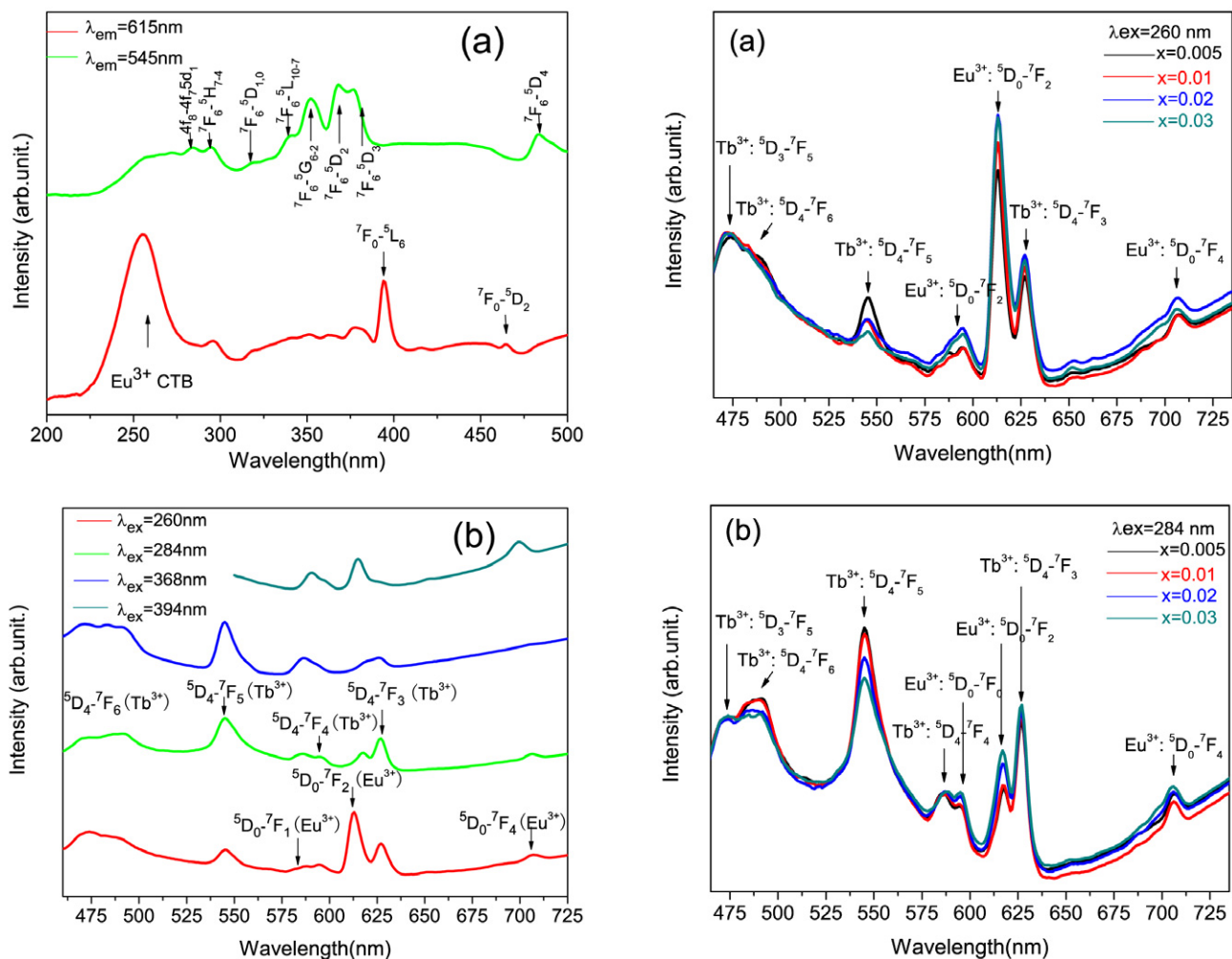


Figure 4. (a) Luminescence excitation spectra of the $Y_{0.965}Tb_{0.03}Eu_{0.005}$ LRH obtained by monitoring the Eu^{3+} emission at 615 nm (red line) and Tb^{3+} emission at 545 nm (green line). (b) Emission spectra of the $Y_{0.965}Tb_{0.03}Eu_{0.005}$ LRH obtained under the different excitation wavelengths indicated in the figure.

A low-magnification TEM image (figure 3(a)) shows the typical flake-like nanocrystals of the $Y_{0.965}Tb_{0.03}Eu_{0.005}$ LRH sample. The hexagonal nanoplates exhibit a relatively wide size distribution and the biggest has a lateral size of ~ 500 nm. Platelets as thin as $\sim 15\text{--}20$ nm are seen in the micrograph. FE-SEM observations indicate that Eu content does not significantly affect the crystal morphology (figure S5). High-resolution TEM (HR-TEM) analysis clearly resolves lattice fringes of the LRH crystal, and the spacing of 0.312 nm may well correspond to the 220 plane of the host layer (figure 3(b)). Selected area electron diffraction (SAED) yielded well-defined diffraction spots (figure 3(c)), indicating that the object under observation is a well-crystallized single crystal. Indexing the SAED pattern (figure 3(c)) is consistent with the ab plane of the LRH crystal.

To elucidate the optical properties of the Y/Tb/Eu ternary system, two binary LRHs of the $Y_{0.995}Eu_{0.005}$ and $Y_{0.97}Tb_{0.03}$ combinations were synthesized and their PL and PLE spectra are shown in figure S6 (see the supplementary material available from stacks.iop.org/STAM/14/015006/mmedia). The PLE spectrum of the $Y_{0.995}Eu_{0.005}$ LRH obtained

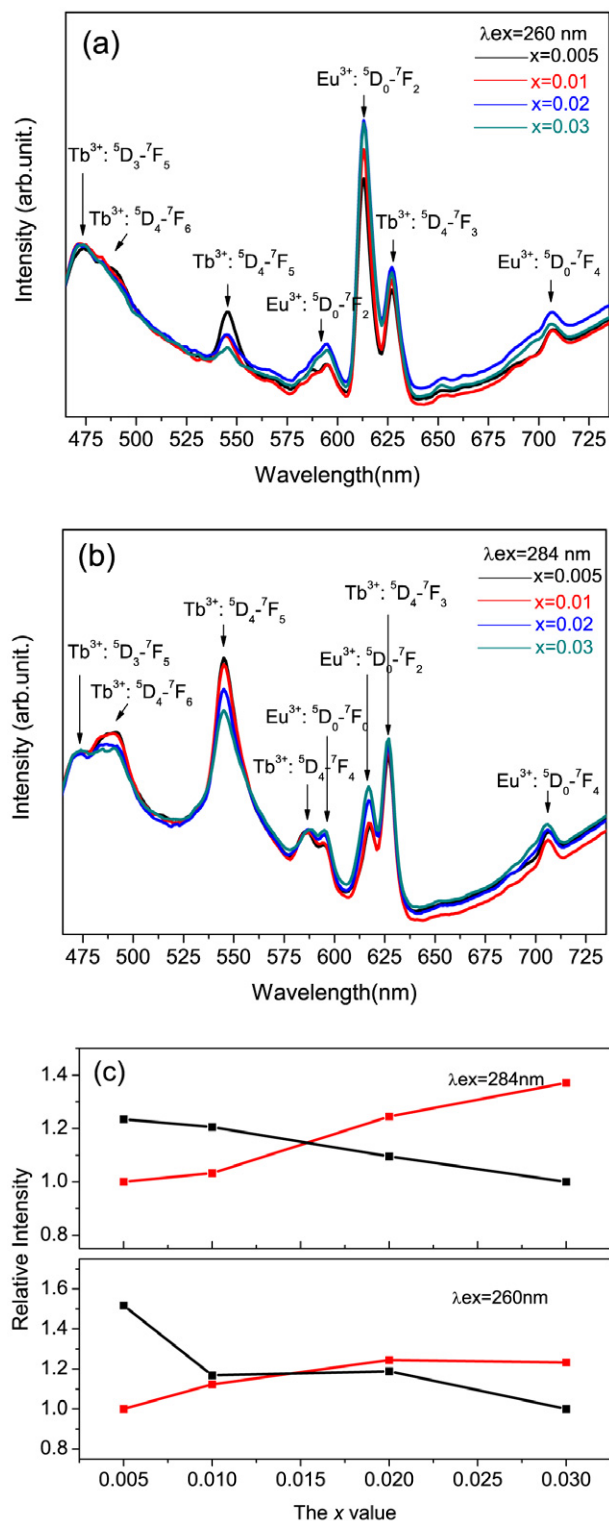


Figure 5. Emission spectra of the $Y_{0.97-x}Tb_{0.03}Eu_x$ LRHs under 260 nm (a) and 284 nm (b) excitation. Panel (c) shows relative intensities of the 615 nm Eu^{3+} and 545 nm Tb^{3+} emissions, as a function of the Eu^{3+} content (the x value).

by monitoring the red emission of Eu^{3+} ions at 615 nm is composed of a relatively strong charge transfer (CT) excitation band at ~ 256 nm and a series of sharp lines in the range 350–550 nm that are ascribed to the intra- $4f^6$ electronic transitions of Eu^{3+} , as labeled in the figure (figure S6(a)).

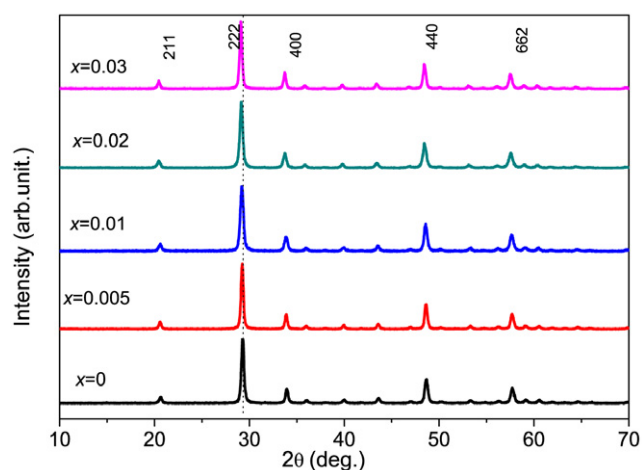


Figure 6. Powder XRD patterns of the $(Y_{0.97-x}Tb_{0.03}Eu_x)_2O_3$ samples calcined from their corresponding LRHs at $1100^\circ C$ for 4 h under flowing NH_3 .

The CT band is assigned to electron transfer from the 2p orbital of O^{2-} to the 4f orbital of Eu^{3+} . Such a strong band was not observed before for the Y/Eu and Gd/Eu binary systems [29, 32] and its origin is still unclear. The PLE of the $Y_{0.97}Tb_{0.03}$ LRH, recorded by monitoring the green emission of Tb^{3+} at 545 nm, exhibits a less-defined broad 4f–5d transition band in the 230–295 nm region [44], along with peaks at 295–500 nm that are attributed to the intra-4f⁸ transitions between the 7F_6 and $^5H_{7-4}$, $^5D_{1,0}$, $^5L_{10-7}$, $^5G_{6-2}$, and $^5D_{2-4}$ levels of Tb^{3+} (figure S6(a)) [45]. The $Y_{0.965}Tb_{0.03}Eu_{0.005}$ ternary LRH shows PLE spectra (figure 4(a)) almost identical to those of the $Y_{0.995}Eu_{0.005}$ and $Y_{0.97}Tb_{0.03}$ binary LRHs for the 615 and 545 nm emissions, respectively, implying that the characteristic emissions of Eu^{3+} and Tb^{3+} can both be obtained by selective excitation.

Photoluminescence spectra of the $Y_{0.995}Eu_{0.005}$ and $Y_{0.97}Tb_{0.03}$ binary LRHs are shown in figure S6(b). Under 394 nm excitation (the $^7F_0 \rightarrow ^5L_6$ transition of Eu^{3+}), the $Y_{0.995}Eu_{0.005}$ sample exhibits characteristic Eu^{3+} emissions at ~ 593 ($^5D_0 \rightarrow ^7F_1$), 615 ($^5D_0 \rightarrow ^7F_2$) and 699 nm ($^5D_0 \rightarrow ^7F_4$). Exciting the $Y_{0.97}Tb_{0.03}$ sample at 368 nm (the $^7F_6 \rightarrow ^5D_2$ transition of Tb^{3+} , the strongest on the PLE curve) yields a strong green band at ~ 545 nm ($^5D_4 \rightarrow ^7F_5$ transition), weaker blue bands at ~ 450 ($^5D_3 \rightarrow ^7F_5$) and 492 nm ($^5D_4 \rightarrow ^7F_6$), and minor red bands at 587 ($^5D_4 \rightarrow ^7F_4$) and 628 nm ($^5D_4 \rightarrow ^7F_3$) [45]. These typical Tb^{3+} emissions are also observed in Tb^{3+} -doped Y_2O_3 [35, 36], Lu_2O_3 [46, 47] and yttrium aluminum garnet (YAG) [48, 49] green phosphors. Tunable emission (figure 4(b)) was achieved with the $Y_{0.965}Tb_{0.03}Eu_{0.005}$ ternary LRH by varying the excitation wavelength from 260 (the CT band of Eu^{3+}) to 394 nm (the $^7F_0 \rightarrow ^5L_6$ transition of Eu^{3+}), showing the advantages of Tb^{3+} and Eu^{3+} codoping. Under 260 nm excitation, the PL spectrum is dominated by Eu^{3+} emissions, along with weaker ones from Tb^{3+} . The Tb^{3+} emission is seen because the excitation wavelength resides on the left slope of the 4f–5d transition band of Tb^{3+} (figure 4(a)). Upon excitation at 284 nm (the $4f^8-4f^75d^1$ transition of Tb^{3+}), the sample exhibits strong Tb^{3+} and weak Eu^{3+} signals. Eu^{3+} emission appears since this

excitation wavelength is located on the right-hand tail of the CT band of Eu^{3+} (figure 4(a)). Only Tb^{3+} and Eu^{3+} peaks were recorded under 368 and 394 nm excitations, respectively, in accordance with the excitation spectra shown in figure 4(a).

The effects of Eu content on photoluminescence of the $Y_{0.97-x}Tb_{0.03}Eu_x$ ternary LRHs are shown in figure 5 for the two typical excitation wavelengths of 260 (figure 5(a)) and 284 nm (figure 5(b)). Irrespective of the x value, strong Eu^{3+} /weak Tb^{3+} and strong Tb^{3+} /weak Eu^{3+} peak combinations were recorded under 260 and 284 nm excitations, respectively, conforming to the results of figure 4(a). The Tb^{3+} emission intensity decreases while that of Eu^{3+} increased with Eu^{3+} content (figure 5(c)), implying the occurrence of energy transfer from Tb^{3+} to Eu^{3+} . The energy transfer rate increased with Eu^{3+} content, thereby affecting the emission intensities of both the activators. Figure 5(c) suggests that the energy transfer is more efficient under 284 nm excitation that corresponds to the $4f^8-4f^75d^1$ transition of Tb^{3+} . Tunable emission colors can thus be obtained with the Tb^{3+} and Eu^{3+} codoped LRHs.

3.2. Characterization and optical properties of the $(Y_{0.97-x}Tb_{0.03}Eu_x)_2O_3$ solid solutions

Tb^{3+} ions readily oxidize at elevated temperatures to form Tb^{4+} , and thus flowing NH_3 (300 ml min^{-1}) was used as a protective/reducing atmosphere upon LRH calcination. The Tb^{3+} -bearing oxides processed up to $900^\circ C$ were light brown, suggesting the presence of Tb^{4+} , while those calcined at $1100^\circ C$ were white. XRD analysis (figure 6) showed that the $1100^\circ C$ samples had high crystallinity and exhibited almost all the diffractions corresponding to the cubic Y_2O_3 (space group: $Ia\bar{3}(206)$, JCPDS no. 89-5591). The d spacing and lattice constant calculated from the 222 diffraction become steadily larger with increasing Eu^{3+} addition (table S3 see the supplementary material available from stacks.iop.org/STAM/14/015006/mmedia), in accordance with the observed gradual shift of the diffraction peak towards the low angles. This result confirms the successful incorporation of larger Eu^{3+} and Tb^{3+} ions into the Y_2O_3 lattice to form solid solutions.

FE-SEM images revealed that the oxides largely retain the thin-plate-like shapes of the original LRH crystals, though some plates have partially collapsed due to the strain arising from thermal decomposition (figures 7(a)–(e)). HR-TEM analysis of the lateral surface of an isolated nanoplate clearly resolved lattice fringes with a spacing of ~ 0.307 nm that corresponds to the 222 crystal plane of the oxide (figure 7(f)). This complies with the findings of Sasaki and co-workers [32], which showed that the host layer (the ab plane) of LRH would quasipototactically transform into the 222 plane of the oxide owing to the similar atomic configurations of the two planes.

Figure 8 shows excitation spectra of the $Y_{0.965}Tb_{0.03}Eu_{0.005}$ ternary and the $Y_{0.995}Eu_{0.005}$ and $Y_{0.97}Tb_{0.03}$ binary solid solution oxides obtained by monitoring the red emission of Eu^{3+} at 613 nm and the green emission of Tb^{3+} at 543 nm. The $Y_{0.995}Eu_{0.005}$

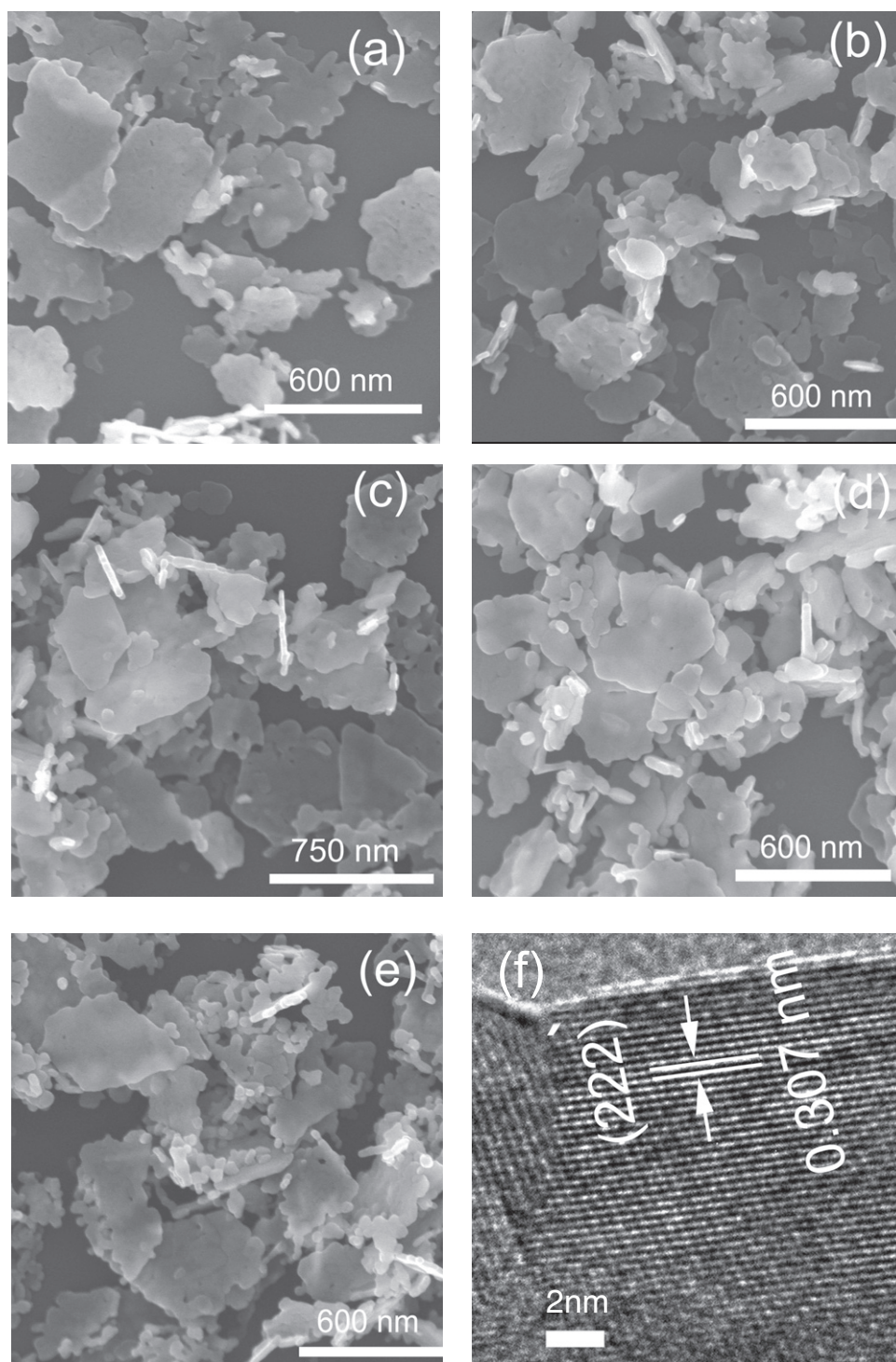


Figure 7. FE-SEM (a)–(e) and HR-TEM (f) images of the $(Y_{0.97-x}Tb_{0.03}Eu_x)_2O_3$ solid solutions calcined under flowing NH_3 at $1100^\circ C$ for 4 h. Panels (a)–(e) correspond to $x = 0, 0.005, 0.01, 0.02$ and 0.03 , respectively; the same sample was used for panels (b) and (f).

sample (spectrum c) shows a sharp and strong CT band at ~ 250 nm, together with a weak host excitation band at ~ 212 nm, as widely observed for Eu^{3+} -doped Y_2O_3 red phosphors [5]. The $Y_{0.97}Tb_{0.03}$ sample exhibits a broad and strong excitation band in the range of ~ 225 – 320 nm, corresponding to the well-documented $4f^8-4f^75d^1$ Tb^{3+} transition (spectrum d) [35]. The doublet at ~ 278 and 303 nm arises from the low-spin and high-spin inter-configurational

$f-d$ transitions of Tb^{3+} electrons, respectively [26, 50]. Unlike their LRH counterparts, the oxides show negligible excitations at longer wavelengths, indicating that the most efficient Eu^{3+} and Tb^{3+} emissions can be obtained through exciting the CT and $4f^8-4f^75d^1$ transition bands, respectively. Monitoring the 543 nm green emission of Tb^{3+} in the $Y_{0.965}Tb_{0.03}Eu_{0.005}$ ternary sample yielded a PLE spectrum (curve (b)) almost identical to that of the $Y_{0.97}Tb_{0.03}$ (curve

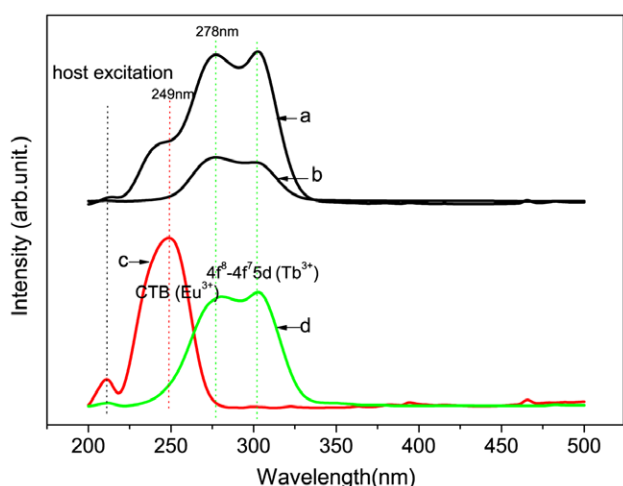


Figure 8. Luminescence excitation spectra of the $Y_{0.965}Tb_{0.03}Eu_{0.005}$ (a, b), $Y_{0.995}Eu_{0.005}$ (c) and $Y_{0.97}Tb_{0.03}$ (d) oxides recorded by monitoring the 613 nm Eu^{3+} emission (a, c) and 543 nm Tb^{3+} emission (b, d).

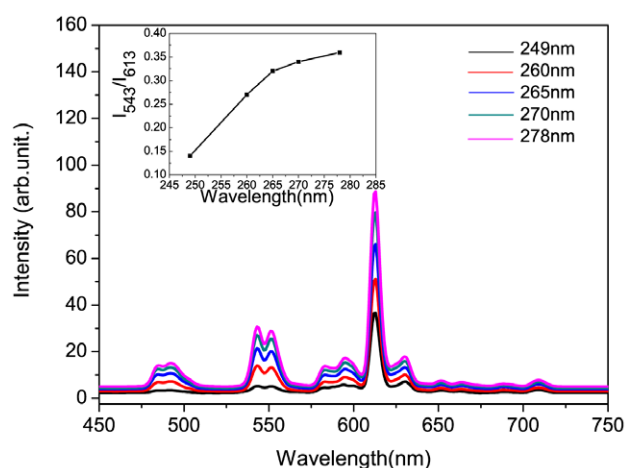


Figure 9. Emission spectra of the $Y_{0.965}Tb_{0.03}Eu_{0.005}$ solid solution oxide under the various excitation wavelengths indicated in the figure. Inset shows the intensity ratio of the green to red emission (I_{543}/I_{613}) as a function of excitation wavelength.

(d). Monitoring the 613 nm Eu^{3+} emission of the same sample, however, produced both the f–d transition band of Tb^{3+} and the CT band of Eu^{3+} in the PLE spectrum (curve (a)), with the former even significantly stronger than the latter. This provides persuasive evidence of an efficient energy transfer from Tb^{3+} to Eu^{3+} , and predicts that stronger Eu^{3+} luminescence can be achieved by exciting the Tb^{3+} ions at 278 or 303 nm rather than through the CT band at ~ 250 nm.

Figure 9 shows the effects of excitation wavelength (249–278 nm) on the luminescence of $Y_{0.965}Tb_{0.03}Eu_{0.005}$ oxide. The PL spectra exhibit similar features irrespective of the excitation wavelength and are composed of two major emission bands at ~ 595 (${}^5D_0 \rightarrow {}^7F_1$) and 615 nm (${}^5D_0 \rightarrow {}^7F_2$) for Eu^{3+} and at ~ 485 (${}^5D_4 \rightarrow {}^7F_4$) and 543 nm (${}^5D_4 \rightarrow {}^7F_3$) for Tb^{3+} . The Tb^{3+} and Eu^{3+} activators can thus be simultaneously excited by UV light. The emission intensity of both Tb^{3+} and Eu^{3+} increases with increasing excitation wavelength. The increase for Tb^{3+} is readily understandable,

since the excitation becomes closer to the center of the strong f–d transition band of Tb^{3+} (figures 8(a) and (d)). The enhancement of Eu^{3+} emission, despite moving the excitation away from the center of the CT band, is clearly due to the energy transfer from Tb^{3+} to Eu^{3+} . Plotting the intensity ratio of the green to red emission (I_{543}/I_{615}) against the excitation wavelength shows that, though the red emission is dominant in each case, green emission gradually gains intensity at longer excitation wavelengths up to 278 nm (figure 9, inset). Color-tunable emission can thus be obtained via selective excitation of the $Y_{0.965}Tb_{0.03}Eu_{0.005}$ sample. When excited at 249, 260, 265, 270 and 278 nm, the sample has CIE chromaticity coordinates of (0.48,0.39), (0.47,0.42), (0.46,0.42), (0.46,0.43) and (0.46,0.43), respectively. All these emission colors fall into the yellow to greenish-yellow region of the CIE chromaticity diagram but with different proportions of green.

The effects of Eu content (the x value) on photoluminescence of the $Y_{0.97-x}Tb_{0.03}Eu_x$ oxides were investigated by exciting the $4f^8-4f^75d^1$ transition of Tb^{3+} at 278 nm, and the results are shown in figure 10(a) with the $Y_{0.995}Eu_{0.005}$ spectrum included for comparison. The $Y_{0.97}Tb_{0.03}$ sample ($x = 0$) exhibits the typical emission of Tb^{3+} in Y_2O_3 and is characterized by strong bands at ~ 543 nm (${}^5D_4 \rightarrow {}^7F_3$ transition, green emission) and ~ 485 nm (${}^5D_4 \rightarrow {}^7F_4$ transition, blue emission). The $Y_{0.995}Eu_{0.005}$ binary sample only produces weak Eu^{3+} emissions because the excitation wavelength of 278 nm falls on the tail of the Eu^{3+} CT band (figure 8, curve (c)), as mentioned above. In the presence of only 0.5 at. % Eu^{3+} ($Y_{0.965}Tb_{0.03}Eu_{0.005}$), the intensity of the 543 nm green emission of Tb^{3+} was drastically reduced to $\sim 21\%$ of the Eu-free sample. Meanwhile the 613 nm Eu^{3+} emission increased \sim seven-fold compared to the $Y_{0.995}Eu_{0.005}$ oxide, indicating a very efficient energy transfer from Tb^{3+} to Eu^{3+} . The Tb^{3+} signals gradually weakened with increasing x whereas the Eu^{3+} emission showed a maximum at $x = 0.01$.

Figure 10(b) shows the relative intensities of luminescence and the red-to-green intensity ratio (I_{613}/I_{543}) for the $Y_{0.97-x}Tb_{0.03}Eu_x$ series. The maximum I_{613}/I_{543} value of ~ 8.6 is observed for $x = 0.02$. The Tb^{3+} to Eu^{3+} energy transfer and the varied emission intensities of both the activators conform well to the PLE spectra obtained by monitoring the 613 and 545 nm emissions (figure S7 see the supplementary material available from stacks.iop.org/STAM/14/015006/mmedia). The optimal activator concentration in Y_2O_3 is ~ 5 at. % for either Tb^{3+} or Eu^{3+} [35, 36], and this value would also hold for the Tb^{3+}/Eu^{3+} codoped system. At the maximum Eu^{3+} emission intensity, the total activator concentration C_{Tb+Eu} of 4 at. % is indeed close to 5 at. %. Overdoping leads to the concentration quenching of luminescence via two mechanisms: (i) shortened separation among the neighboring activators, if a uniform dopant distribution was assumed, and (ii) localized dopant distribution (dopant clustering) owing to the lattice strain induced by surplus incorporation of larger Tb^{3+} and especially Eu^{3+} ions. Concentration quenching of luminescence was not observed for the LRHs in this and previous studies

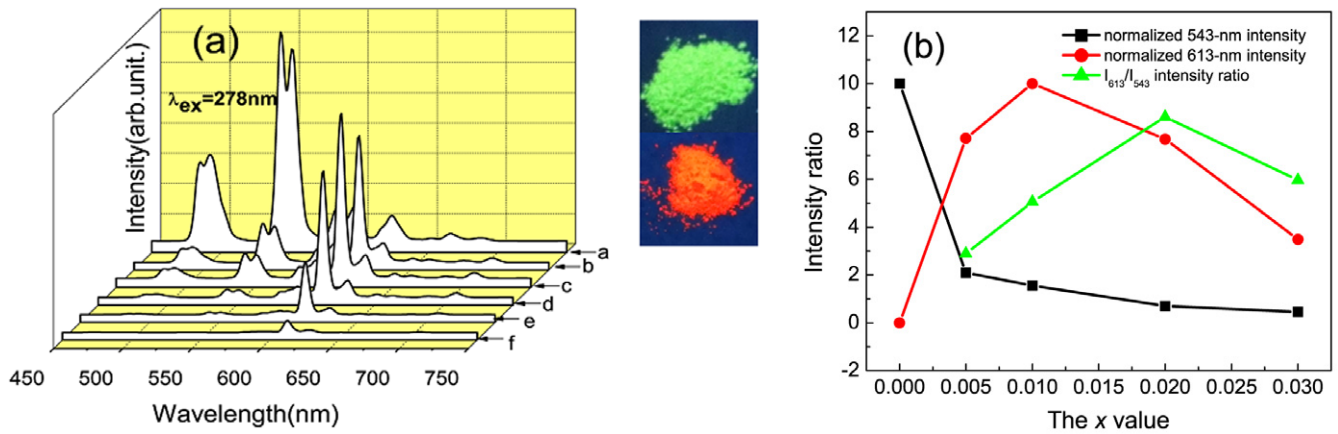


Figure 10. (a) Emission spectra of the $Y_{0.97-x}Tb_{0.03}Eu_x$ ternary oxides under 278 nm excitation for $x = 0, 0.005, 0.01, 0.02$ and 0.03 (curves (a)–(e), respectively). Curve (f) corresponds to the $Y_{0.995}Eu_{0.005}$ oxide and is included for comparison. The right part shows luminescence of the $x = 0$ and 0.10 samples under 254 nm excitation from a hand-held UV lamp. (b) Intensities of the 543 and 613 nm emissions normalized to 10, and the I_{613}/I_{543} intensity ratio versus Eu content (the x value).

Table 1. Fluorescence lifetimes of the 543 nm Tb^{3+} and 613 nm Eu^{3+} emissions for the $(Y_{0.97-x}Tb_{0.03}Eu_x)_2O_3$ nanoplates, τ_R (Tb^{3+}) and τ_R (Eu^{3+}), respectively.

x	0	0.005	0.01	0.02	0.03
τ_R (Tb^{3+}) ms	3.03 ± 0.01	2.10 ± 0.01	1.89 ± 0.01	1.47 ± 0.01	1.44 ± 0.01
τ_R (Eu^{3+}) ms	–	2.56 ± 0.01	2.33 ± 0.01	2.27 ± 0.01	2.04 ± 0.01

[28, 29, 32] because in the LRH structure the activators reside at the centers of the $[Ln(OH)_7(H_2O)]$ and $[Ln(OH)_8(H_2O)]$ polyhedrons and are well separated from each other. The maximum I_{613}/I_{543} ratio at $x = 0.02$ ($C_{Tb+Eu} = 5$ at.%) observed in figure 10(b) might result from an interplay between the efficiency of Tb^{3+} to Eu^{3+} energy transfer and the relative extent of concentration quenching between Tb^{3+} and Eu^{3+} emissions. In the absence of concentration quenching, the efficiency of Tb^{3+} to Eu^{3+} energy transfer (η_{ET}) can be calculated from the fluorescence intensity using the formula [51–53]

$$\eta_{ET} = 1 - \frac{I_S}{I_{S0}}, \quad (1)$$

where I_S and I_{S0} are the integrated intensities of Tb^{3+} emission in the presence and in the absence of Eu^{3+} , respectively. Using the experiment results of figure 10(a) and equation (1) the η_{ET} values were estimated at $\sim 86\%$ for $x = 0.005$ and 91% for $x = 0.01$. These high efficiencies of energy transfer primarily originate from the significant spectral overlap between the ${}^5D_4 \rightarrow {}^7F_j$ emission of Tb^{3+} and the ${}^7F_{0,1} \rightarrow {}^5D_{0,1,2}$ absorption of Eu^{3+} [54]. The Tb^{3+} to Eu^{3+} energy transfer may occur via exchange interaction and electric multipole interaction; it depends on the average distance (R) between the Tb^{3+} donor and Eu^{3+} acceptor ions. Exchange interaction generally requires an overlap of the donor and acceptor orbitals and an R value of less than $0.3\text{--}0.4$ nm; otherwise, the electric multipole interaction may dominate [55]. The average separation R can be estimated from the following equation proposed by Blasse and Bril [56, 57]

$$R \approx 2 \left(\frac{3V}{4\pi C_{Tb+Eu} N} \right)^{1/3}, \quad (2)$$

where C_{Tb+Eu} is the total concentration of Tb^{3+} and Eu^{3+} ions, N is the number of sites that the rare-earth ions can occupy per unit cell and V is the cell volume. Cubic Y_2O_3 has 80 atoms per unit cell, among which 32 are cations, and therefore $N = 32$ [5, 58]. With the cell volume shown in table S3, calculations according to equation (2) yield $R = 1.328, 1.262, 1.209, 1.125$ and 1.061 nm for $C_{Tb+Eu} = 0.03, 0.035, 0.04, 0.05$ and 0.06 , respectively. All these values are significantly larger than the $0.3\text{--}0.4$ nm required for the exchange interaction mechanism, implying that the Tb^{3+} to Eu^{3+} energy transfer largely takes place via electric multipole interactions.

The oxide nanoplates exhibit vivid luminescence colors under 254 nm UV excitation, as shown in figure S8 for all the compositions and in the right part of figure 10(a) for two typical ones. Color-tunable photoluminescence was thus achieved with the $Y_{0.97-x}Tb_{0.03}Eu_x$ phosphors by varying the Eu content, and the CIE chromaticity coordinates (x, y) of the emissions were $(0.34, 0.53)$ for $x = 0$, $(0.46, 0.43)$ for $x = 0.005$, $(0.48, 0.41)$ for $x = 0.01$, $(0.50, 0.39)$ for $x = 0.02$, and $(0.49, 0.39)$ for $x = 0.03$, roughly corresponding to yellowish-green, yellow, yellowish-orange, yellowish-orange and yellowish-white colors, respectively.

Fluorescence kinetics were studied for the ${}^5D_0 \rightarrow {}^7F_2$ emission of Eu^{3+} at 613 nm and the ${}^5D_4 \rightarrow {}^7F_5$ transition of Tb^{3+} at 543 nm. The decay curves (figure S9) can be fitted with the single-exponential function of $I = A \exp(-t/\tau_R) + B$, where τ_R is the fluorescence lifetime, t is delay time, I is relative intensity and A and B are constants, and the derived fluorescence lifetimes are summarized in table 1. The lifetime of Eu^{3+} emission slowly yet continuously decreases with increasing Eu content, which might be understood from

the following two aspects. Raising the Eu concentration shortens the separation among the luminescent centers, which increases the probability of non-radiative energy transfer among them via electric multipole interactions. It also increases the probability of radiative (resonant) energy transfer among the Eu^{3+} ions followed by non-radiative transfer to the surface sites. Both mechanisms shorten the fluorescence lifetime. The fluorescence lifetime of Tb^{3+} emission rapidly decreases from 3.03 ms for $x = 0$ to 2.10 ms for $x = 0.005$ and then to 1.89 ms for $x = 0.01$ due to the energy transfer from Tb^{3+} to Eu^{3+} , which is frequently observed for donor/acceptor codoped systems [54, 59]. Beside the Tb^{3+} to Eu^{3+} energy transfer, other mechanisms such as defect clustering due to lattice strain (mechanism (2) mentioned above for Eu^{3+}) may contribute to the lifetime shortening at larger x values.

4. Conclusions

Multicolor phosphor nanoplates of the Y/Tb/Eu system were produced by optimized hydrothermal synthesis of $(\text{Y}_{0.97-x}\text{Tb}_{0.03}\text{Eu}_x)_2(\text{OH})_5\text{NO}_3 \cdot n\text{H}_2\text{O}$ LRHs and $(\text{Y}_{0.97-x}\text{Tb}_{0.03}\text{Eu}_x)_2\text{O}_3$ solid solutions ($x = 0-0.03$). Detailed characterization by XRD, FTIR, FE-SEM, TEM and optical spectroscopies yielded the following conclusions:

1. Phase-pure LRH can be obtained at pH ~ 7.0 and 100°C , whereas mixtures of high-hydration and low-hydration phases were produced at higher temperatures up to 200°C .
2. Irrespective of the hydration extent, the LRHs are solid solutions with free NO_3^- anions intercalated between the layers. The incorporation of relatively large Eu^{3+} and Tb^{3+} ions expands the ab planes while reducing the hydration degree and the interlayer distance.
3. Characteristic Tb^{3+} and Eu^{3+} emission lines are observed from ternary LRHs when selectively exciting the two types of activators, and the occurrence of energy transfer from Tb^{3+} to Eu^{3+} was confirmed.
4. The $(\text{Y}_{0.97-x}\text{Tb}_{0.03}\text{Eu}_x)_2\text{O}_3$ solid-solution nanoplates annealed from the LRHs at 1100°C possess exposed 222 facets. The color and intensity of luminescence can be tuned by varying the excitation wavelength from ~ 249 nm (the charge transfer excitation band of Eu^{3+}) to 278 nm (the $4f^8-4f^75d^1$ transition of Tb^{3+}).
5. Efficient Tb^{3+} to Eu^{3+} energy transfer was observed for the $(\text{Y}_{0.97-x}\text{Tb}_{0.03}\text{Eu}_x)_2\text{O}_3$ phosphor, allowing one to tune the emission color from approximately green to yellowish-orange by varying the $\text{Eu}^{3+}/\text{Tb}^{3+}$ atomic ratio.
6. At the optimal Eu^{3+} content of $x = 0.01$ for $(\text{Y}_{0.97-x}\text{Tb}_{0.03}\text{Eu}_x)_2\text{O}_3$, the efficiency of energy transfer was $\sim 91\%$, and the transfer was attributed to electric multipole interactions.

Acknowledgments

This work was supported by the National Natural Science Foundation of China (grant numbers 50972025 and

51172038) and the Special Fund for Fundamental Research in Central Universities (grant numbers N110802001 and N100702001). Sincere thanks are due to Dr Renzhi Ma, World Premier International Center for Materials Nanoarchitectonics (MANA), National Institute for Materials (NIMS), for performing TEM analysis. X L Wu would like to thank NIMS for granting a NIMS Internship. We acknowledge the Program for New Century Excellent Talents in University (NCET-11-0076).

References

- [1] Ekambaran S, Patil K C and Maaza M 2005 *J. Alloys Compounds* **393** 81
- [2] Igarashi T, Ihara M, Kusunoki T, Ohno K, Isobe T and Senna M 2000 *Appl. Phys. Lett.* **76** 1549
- [3] Dhanaraj J, Jagannathan R, Kutty T R N and Lu C H 2001 *J. Phys. Chem. B* **105** 11098
- [4] Li J-G, Ikegami T, Mori T and Yajima Y 2003 *J. Am. Ceram. Soc.* **86** 1493
- [5] Li J-G, Li X D, Sun X D and Ishigaki T 2008 *J. Phys. Chem. C* **112** 11707
- [6] Li J-G, Li X D, Sun X, Ikegami T and Ishigaki T 2008 *Chem. Mater.* **20** 2274
- [7] Li J-G, Zhu Q, Li X D, Sun X D and Sakka Y 2011 *Acta Mater.* **59** 3688
- [8] Ropp R C 1993 *The Chemistry of Artificial Lighting Devices: Lamps, Phosphors and Cathode Ray Tubes* (New York: Elsevier)
- [9] Bhargava R N 1996 *J. Lumin.* **70** 85
- [10] Ebendorff-Heidepriem H and Ehrtd D 1999 *J. Non-Cryst. Solids* **248** 247
- [11] Kawahara Y, Petrykin V, Ichihara T, Kijima N and Kakihana M 2006 *Chem. Mater.* **18** 6303
- [12] Jadhav A P, Kim C W, Cha H G, Pawar A U, Jadhav N A, Pal U and Kang Y S 2009 *J. Phys. Chem. C* **113** 13600
- [13] Flores-Gonzalez M A, Villanueva-Ibanez M and Bazzi R 2009 *Bol. Soc. Esp. Ceram. V.* **48** 141
- [14] Meng Q et al 2007 *J. Appl. Phys.* **102** 093505
- [15] Feldmann C and Merikhi J 2003 *J. Mater. Sci.* **38** 1731
- [16] Song H W, Yu L X, Yang L M and Lu S Z 2005 *J. Nanosci. Nanotechnol.* **5** 1519
- [17] Devaraju M K, Yin S and Sato T 2009 *Nanotechnology* **20** 305302
- [18] Zhong S, Wang S, Xu H, Hou H, Wen Z, Li P, Wang S and Xu R 2009 *J. Mater. Sci.* **44** 3687
- [19] Zhu H, Ma Y, Yang H, Zhu P, Du J, Ji C and Hou D 2010 *Solid State Commun.* **150** 1208
- [20] Setua S, Menon D, Asok A, Nair S and Koyakutty M 2010 *Biomaterials* **31** 714
- [21] Gandara F, Perles J, Snejko N, Iglesias M, Gomez-Lor B, Gutierrez-Puebla E and Monge M A 2006 *Angew. Chem. Int. Edn Engl.* **45** 7998
- [22] McIntyre L J, Jackson L K and Fogg A M 2008 *Chem. Mater.* **20** 335
- [23] McIntyre L J, Jackson L K and Fogg A M 2008 *J. Phys. Chem. Solids* **69** 1070
- [24] Poudret L, Prior T J, McIntyre L J and Fogg A M 2008 *Chem. Mater.* **20** 7447
- [25] Lee K H and Byeon S H 2009 *Eur. J. Inorg. Chem.* **7** 929
- [26] Geng F X, Matsushita Y, Ma R Z, Xin H, Tanaka M, Izumi F, Iyi N and Sasaki T 2008 *J. Am. Chem. Soc.* **130** 16344
- [27] Geng F X, Matsushita Y, Ma R Z, Xin H, Tanaka M, Iyi N and Sasaki T 2009 *Inorg. Chem.* **48** 6724
- [28] Geng F X, Xin H, Matsushita Y, Ma R Z, Tanaka M, Izumi F, Iyi N and Sasaki T 2008 *Chem. Eur. J.* **14** 9255

- [29] Zhu Q, Li J-G, Zhi C Y, Li X D, Sun X D, Sakka Y, Golberg D and Bando Y 2010 *Chem. Mater.* **22** 4204
- [30] Wu X L, Li J-G, Zhu Q, Li J K, Ma R Z, Sasaki T, Li X D, Sun X D and Sakka Y 2012 *Dalton Trans.* **41** 1854
- [31] Hu L F, Ma R Z, Ozawa T C, Geng F X, Iyi N and Sasaki T 2008 *Chem. Commun.* **40** 4897
- [32] Hu L F, Ma R Z, Ozawa T C and Sasaki T 2009 *Angew. Chem. Int. Edn. Engl.* **48** 3846
- [33] Hu L F, Ma R Z, Ozawa T C and Sasaki T 2010 *Inorg. Chem.* **49** 2960
- [34] Zhu Q, Li J-G, Zhi C Y, Ma R Z, Sasaki T, Xu J X, Liu C H, Li X D, Sun X D and Sakka Y 2011 *J. Mater. Chem.* **21** 6903
- [35] Flores-Gonzalez M A, Ledoux G, Roux S, Lebbou K, Perriat P and Tillement O 2005 *J. Solid State Chem.* **178** 989
- [36] Ray S, Patra A and Pramanik P 2007 *Opt. Mater.* **30** 608
- [37] McIntyre L J, Prior T J and Fogg A M 2010 *Chem. Mater.* **22** 2635
- [38] Geng F X, Ma R Z and Sasaki T 2010 *Acc. Chem. Res.* **43** 1177
- [39] Lee K-H and Byeon S H 2009 *Eur. J. Inorg. Chem.* **31** 4727
- [40] Lee K-H, Lee B-I, You J-H and Byeon S-H 2010 *Chem. Commun.* **46** 1461
- [41] Nakamoto K 1978 *Infrared and Raman Spectra of Inorganic and Coordination Compounds* (New York: Wiley)
- [42] Sandford S A 1984 *Icarus* **60** 115
- [43] Shannon R D 1976 *Acta Crystallogr. A* **32** 751
- [44] Liu Y, Qian G D, Wang Z Y and Wang M Q 2005 *Appl. Phys. Lett.* **86** 71907
- [45] Wang L, Yan D P, Qin S H, Li S D, Lu J, Evans D G and Duan X 2011 *T Dalton Trans.* **40** 11781
- [46] Makhov V N, Lushchik C, Lushchik A, Kirm M, Wang Z F, Zhang W P, Yin M and Zhao J T 2009 *J. Lumin.* **129** 1711
- [47] Trojan-Piegza J, Zych E, Hölsä J and Niittykoski J 2009 *J. Phys. Chem. C* **113** 20493
- [48] Robbins D J, Cockayne B, Lent B and Glasper J L 1976 *Solid State Commun.* **20** 673
- [49] Van der Weg W F, Popma T J A and Vink A T 1985 *J. Appl. Phys.* **57** 5450
- [50] Dorenbos P 2000 *J. Lumin.* **91** 155
- [51] Kumar G A, Biju P R, Jose G and Unnikrishnan N V 1999 *Mater. Chem. Phys.* **60** 247
- [52] Paulose P I, Jose G, Thomas V, Unnikrishnan N V and Warriar M K R 2003 *J. Phys. Chem. Solids* **64** 841
- [53] Rai S and Hazarika S 2008 *Opt. Mater.* **30** 1343
- [54] Di W, Wang X, Zhu P and Chen B 2007 *J. Solid State Chem.* **180** 467
- [55] Dexter D L and Schulman J H 1954 *Chem. Phys.* **22** 1063
- [56] Blasse G and Brill A 1969 *J. Chem. Phys.* **51** 3252
- [57] Blasse G 1986 *J. Solid State Chem.* **62** 207
- [58] Gaboriaud R J, Pailloux F, Guerin P and Paumier F 2000 *J. Phys. D: Appl. Phys.* **33** 2884
- [59] Mukherjee S, Sudarsan V, Vatsa R K, Godbole S V, Kadam R M, Bhatta U M and Tyagi A K 2008 *Nanotechnology* **19** 325704